Self-consistent transit time model for a resonant tunnel diode

Yun Zheng and Roger Lake

Abstract

A self-consistent analytic expression for the small-signal impedance model of a resonant tunnel diode (RTD) with a finite transit time through the collector is presented. The effect of the collector transit time on the device impedance is described for 3 $In_{0.53}Ga_{0.47}As$/AlAs/InAs RTDs with current densities ranging from 10 kA/cm^2 to 430 kA/cm^2 for DC biasing in both the positive and negative differential resistance regions.

Index Terms

Resonant tunnel diode (RTD), small-signal impedance model, transit time diode, millimeter wave, microwave

I. INTRODUCTION

A resonant tunnel diode (RTD) can provide a current injection angle to a transist time region in the collector and act as a negative dynamical resistance transit time device [1]–[3]. At frequencies such that the injection plus transit time angle is about 2π the device exhibits negative dynamical resistance even when the DC bias of the RTD is in the positive differential resistance (PDR) region. An RTD biased in this manner for use as a local oscillator (LO) has several appealing characteristics compared to an RTD biased in the negative differential resistance (NDR) region: (i) the dynamical resistance only becomes negative at frequencies around the 2π current angle so that the LO is not a wideband oscillator that can oscillate down to zero frequency; (ii) DC

Y. Zheng and R. Lake are with the Department of Electrical Engineering, University of California, Riverside, CA 92521-0204 USA. (corresponding author R. Lake; rlake@ee.ucr.edu)

This work was supported by Raytheon, the NSF, and UCR.

biasing of the RTD is much easier since the bias point is in the PDR region; (iii) output power is increased since the PDR region spans a larger voltage range, ΔV, than the NDR region, and the inclusion of a transit time region further increases ΔV.

For RTDs DC biased in the NDR region, a collector depletion region is often designed to reduce the device capacitance. Below, we analyze the collector transit time effects in both the NDR and PDR bias modes for $In_{0.53}Ga_{0.47}As$/AlAs/InAs RTDs with current densities ranging from 10 kA/cm^2 to 430 kA/cm^2. We plot the maximum negative resistance that can be obtained at frequencies of 30 - 300 GHz for RTDs DC biased in the PDR region. We show the frequency response of the negative resistance for RTDs DC biased in the NDR region with a series of different collector lengths.

Our approach is to solve a self-consistent model consisting of a δ-depletion type charge distribution as shown in Fig. 1 combined with a rate-equation model for the RTD. The RTD is divided into an injection region and a drift region. Using small signal analysis, we derive impedance models for each region. If we were to ignore the collector transit time effects, our model for the RTD would result in equations for the small signal impedance identical to those of Feiginov [4]. If we were to ignore charging of the well, our model for the drift region impedance would be identical to previous models [2], [3], [5], [6].

II. Injection Region Impedance Model

The band diagram of an RTD is shown in Fig. 1, where the RTD has been divided into the injection region and the drift region. J_{ew} represents the emitter-to-well tunneling current density and J_{wc} represents the well-to-collector tunneling current density. l is the collector barrier thickness plus the half width of the QW and d is the emitter barrier thickness plus the half width of the QW. The potential in the well is denoted as V_w, and V_0 is the potential at the right edge of the collector barrier. Underneath the band diagram is the simplified space charge distribution. We assume the charge distributions in the QW and emitter regions are delta functions of charge, where n_w and n_e are used to denote the two-dimensional (2D) electron concentration in the well and emitter, respectively.

Within the injection region, we integrate the two delta charge distributions to obtain the electric field distribution, and we integrate the electric field to obtain the voltage. Two expressions for the voltage in the well, Eqs. (1) and (2), are obtained by integrating the electric field from left

and the right, respectively.

$$V_w = \frac{qn_e}{\epsilon} d, \tag{1}$$

$$V_w = V_0 - \frac{q\left(n_e + n_w\right)}{\epsilon} l. \tag{2}$$

Using Eqs. (1) and (2), we write V_w and n_e in terms of the electron density in the well, n_w, and the potential at the beginning of the drift region, V_0. We will then use the current and continuity equations to solve for n_w in terms of V_0. Substituting Eq. (1) into Eq. (2), we write the potential in the well as

$$V_w = \frac{d}{l+d}\left(V_0 - \frac{l}{\epsilon} q n_w\right). \tag{3}$$

Subtracting Eq. (3) from V_0 gives the voltage drop between the center of the well and the beginning of the drift region, $V_{0w} = V_0 - V_w$,

$$V_{0w} = \frac{l}{l+d}\left(V_0 + \frac{d}{\epsilon} q n_w\right). \tag{4}$$

Substituting Eq. (2) into (1), we write n_e as

$$n_e = \frac{\epsilon}{q(l+d)} V_0 - \frac{l}{l+d} n_w. \tag{5}$$

The particle current flowing from the emitter to well is $J_{ew} = q\left(n_e - n_w\right)\Gamma_e$, and the particle current flowing from the well to the collector is $J_{wc} = qn_w\Gamma_c$ where we ignore back injection from the collector. The continuity equation is $q\partial n_w/\partial t = J_{ew} - J_{wc}$ where Γ_e and Γ_c are the electron escape rates (s^{-1}) due to the tunneling to emitter and collector, respectively. Γ_e and Γ_c are bias-dependent.

We now use small signal analysis and write all physical quantities as the sum of a DC term and an AC term with a complex amplitude. For example, the voltage in the well is written as $V_w = V_w^0 + \tilde{V}_w e^{j\omega t}$ where V_w^0 is the DC term and $\tilde{V}_w$ is the complex AC amplitude. We then equate the time dependent terms and cancel the time dependent $e^{j\omega t}$ factor keeping only first order terms in the AC amplitudes.

From equations for J_{ew} and J_{wc} we obtain the linearized small-signal equations for the currents $\tilde{J}_{ew}$ and $\tilde{J}_{wc}$.

$$\tilde{J}_{ew} = q\Gamma_e^0\left(\tilde{n}_e - \tilde{n}_w\right) + q\left(n_e^0 - n_w^0\right)\Gamma_e'\tilde{V}_w, \tag{6}$$

$$\tilde{J}_{wc} = q\Gamma_c^0\tilde{n}_w + qn_w^0\Gamma_c'\tilde{V}_{0w}, \tag{7}$$

In Eqs. (6) and (7), $\Gamma'_c \equiv \frac{\partial \Gamma_c}{\partial V_{0w}}$ and $\Gamma'_e \equiv \frac{\partial \Gamma_e}{\partial V_{we}}$. Since the emitter is grounded, $\tilde{V}_{we} = \tilde{V}_w$. The small signal continuity equation becomes

$$j\omega q \tilde{n}_w = \tilde{J}_{ew} - \tilde{J}_{wc}, \tag{8}$$

Starting with the AC continuity equation, Eq. (8), substituting in the expressions for $\tilde{J}_{ew}$ and $\tilde{J}_{wc}$ from Eqs. (6) and (7) and then substituting in the expressions for $\tilde{V}_w$, $\tilde{V}_{0w}$, and $\tilde{n}_e$ from Eqs. (3) - (5), we obtain the proportionality between $\tilde{n}_w$ and $\tilde{V}_0$.

$$\tilde{n}_w = \frac{\frac{1}{q}\left[C_{w0}(\Gamma - \Gamma_0) - q n_w^0 \Gamma'_c\right]}{j\omega + \Gamma} \cdot \tilde{V}_0, \tag{9}$$

$C_{w0} = \epsilon/l$ is the well-collector capacitance per unit area. We also define here the parallel well-collector / well-emitter capacitance per unit area, $C = \epsilon(1/l + 1/d)$, and the emitter-collector capacitance per unit area, $C_{e0} = \epsilon/(l+d)$. $\Gamma_0 = \Gamma_e^0 + \Gamma_c^0$ is the inverse intrinsic electron lifetime in the well. The quantity Γ is defined as

$$\Gamma = \Gamma_e^0 + \Gamma_c^0 + \frac{l}{l+d}\Gamma_e^0 + \frac{q\left(n_e^0 - n_w^0\right)}{C}\Gamma'_e + \frac{q n_w^0}{C}\Gamma'_c. \tag{10}$$

To obtain the small-signal impedance of the injection region, we require the relationship between the total current density, $\tilde{J}$, and the voltage across the injection region, $\tilde{V}_0$. The total current $\tilde{J}$ is the sum of the particle current ($\tilde{J}_p$) and the displacement current ($\tilde{J}_d$), $\tilde{J} = \tilde{J}_p(x) + \tilde{J}_d(x)$. Since the total current is continuous, independent of position, we evaluate the particle current and displacement current at $x = 0$, the interface of the injection and drift regions.

$$\tilde{J}_p(x=0) = q\Gamma_c^0 \tilde{n}_w + q n_w^0 \Gamma'_c \tilde{V}_{0w}, \tag{11}$$

$$\tilde{J}_d(x=0) = -j\omega\epsilon\tilde{\mathcal{E}}(x=0) = j\omega q\left(\tilde{n}_e + \tilde{n}_w\right). \tag{12}$$

Note that the negative sign in Eq. (12) converts the physics sign convention determined by direction along the x axis to the circuit sign convention in which positive current flows from the positive voltage V_0 at the right. We can write $\tilde{J}$ as a function of $\tilde{V}_0$ by substituting Eqs. (4), (5) and (9) into Eqs. (11) and (12) and adding. The impedance of the injection region is then given by

$$\frac{1}{Z_I(\omega)} = \frac{\tilde{J}}{\tilde{V}_0} = j\omega C_{e0} + G^\infty + \frac{G^0 - G^\infty}{1 + j\omega\frac{1}{\Gamma}}, \tag{13}$$

where G^0 is the static conductance,

$$\begin{aligned} G^0 &= \Gamma_c^0 C_{w0}\left(1-\frac{\Gamma_0}{\Gamma}\right)+qn_w^0\Gamma_c'\left(1-\frac{\Gamma_0}{\Gamma}\right) \\ &\quad -\frac{1}{\Gamma}\left[qn_w^0\Gamma_c'\left(\frac{d}{l+d}\Gamma_c^0-\frac{l}{l+d}\Gamma_e^0\right)+\frac{1}{C}\left(qn_w^0\Gamma_c'\right)^2\right] \end{aligned} \tag{14}$$

and G^∞ is the high frequency conductance given by

$$G^\infty = \frac{d}{l+d}C_{w0}\left(\Gamma-\Gamma_0\right)+\frac{l-d}{l+d}qn_w^0\Gamma_c'. \tag{15}$$

Eq. (13) is the same as Eq. (6) of Feiginov [4]. It results in the RLC circuit model [4], [7] for the injection region shown in Fig. (2) with $L_Q = 1/\left[\Gamma\left(G^0-G^\infty\right)\right]$. At low frequencies, $\omega/\Gamma \ll 1$, this model reduces to the parallel quantum capacitance model of [8].

III. Drift Region Impedance Model

The impedance of the drift region is calculated in the usual way as described by Sze [9]. One relates the electric field in the drift region to the displacement current, which is then written in terms of the total current. Integrating the electric field across the drift region gives the voltage drop in terms of the current. The ratio is the impedance.

Assuming that the electrons travel across the drift region at their saturation velocity, v_s, the amplitude of the ac particle current, which is injected into the drift region at the $x=0$ plane is $\tilde{J}_p(x) = \tilde{J}_p(x=0)e^{-j\omega x/v_s}$. The electric field in the drift region is

$$\tilde{\mathcal{E}}(x) = \frac{\tilde{J}_d(x)}{j\omega\epsilon} = \frac{\tilde{J}-\tilde{J}_p(x)}{j\omega\epsilon} = \frac{\tilde{J}-\tilde{J}_p(x=0)e^{-j\omega x/v_s}}{j\omega\epsilon}. \tag{16}$$

At $x=0$, the particle current amplitude is some complex fraction, γ, of the total current, $\tilde{J}_p(x=0) = \gamma\tilde{J}$. Thus, Eq. (16) for the electric field becomes

$$\tilde{\mathcal{E}}(x) = \tilde{J}\left[\frac{1-\gamma e^{-j\omega x/v_s}}{j\omega\epsilon}\right]. \tag{17}$$

Integrating Eq. (17) across the drift region results in the voltage drop and thus, the drift-region impedance,

$$Z_D = \frac{\tilde{V}_{a0}}{\tilde{J}} = \frac{1}{j\omega C_{0c}}\left[1-\frac{\gamma}{j\theta_c}\left(1-e^{-j\theta_c}\right)\right], \tag{18}$$

where $C_{0c} = \frac{\epsilon}{X_c}$ is the capapcitance of the drift region per unit area, and $\theta_c = \omega X_c/v_s$ is the transit angle of the drift region.

The final task is to derive an expression for $\gamma = \tilde{J}_p(x=0)/\tilde{J}$. The total current is given by Eq. (13) which we write over a common denominator,

$$\tilde{J} = \frac{\left(G^0 - \frac{\omega^2}{\Gamma} C_{e0}\right) + \frac{j\omega}{\Gamma}\left(G^\infty + \Gamma C_{e0}\right)}{1 + j\omega\frac{1}{\Gamma}} \cdot \tilde{V}_0, \tag{19}$$

The particle current is found by substituting in the expressions for $\tilde{n}_w$ and $\tilde{V}_{0w}$, Eqs. (9) and (4), into Eq. (11) for the particle current and using the definition of G^0, Eq. (14).

$$\tilde{J}_p(x=0) = \frac{G^0 + \frac{j\omega}{\Gamma}\frac{l}{l+d} q n_w^0 \Gamma_c'}{1 + j\omega\frac{1}{\Gamma}} \cdot \tilde{V}_0. \tag{20}$$

The ratio of Eqs. (20) and (19) gives the value for γ,

$$\gamma = \frac{\tilde{J}_p(x=0)}{\tilde{J}} = \frac{G^0 + \frac{j\omega}{\Gamma}\frac{l}{l+d} q n_w^0 \Gamma_c'}{\left(G^0 - \frac{\omega^2}{\Gamma} C_{e0}\right) + \frac{j\omega}{\Gamma}\left(G^\infty + \Gamma C_{e0}\right)}. \tag{21}$$

Note that γ does not have the simple form of $G^0/\left(G^0 + j\omega\epsilon C_{e0}\right)$ used previously [2], [3], [5], [6]. The displacement current at $x = 0$ is not simply the current through the capacitor in Fig. 2, $j\omega C_{e0}\tilde{V}_0 = j\omega\epsilon\tilde{V}_0/(l+d)$. This would imply that the electric field at $x = 0$ was $\tilde{V}_0/(l+d)$ which would only be true if there were no charging of the well. We have tried both forms, and the self-consistent value of γ, Eq. (21), gives significantly different results from the non-self-consistent value.

IV. RTD Impedance Model

The total impedance for the RTD is the sum of the impedances of the injection region and the drift region,

$$\begin{aligned} Z_{RTD} &= Z_I + Z_D \\ &= \frac{1 + j\omega\frac{1}{\Gamma}}{\left(G^0 - \frac{\omega^2}{\Gamma} C_{e0}\right) + \frac{j\omega}{\Gamma}\left(G^\infty + \Gamma C_{e0}\right)} + \frac{1}{j\omega C_{0c}}\left[1 - \frac{\gamma}{j\theta_c}\left(1 - e^{-j\theta_c}\right)\right]. \end{aligned} \tag{22}$$

The limit of the resistance at zero frequency is

$$Z_{RTD}^0 = \frac{1}{G^0}\left[\frac{l + d + X_c^0}{l+d} + \frac{X_c^0}{l+d}\frac{d}{l}\left(1 - \frac{\Gamma_0}{\Gamma} - \frac{\Gamma_c'}{\Gamma}\frac{l}{\epsilon} q n_w^0\right)\right] + \frac{\left(X_c^0\right)^2}{2\epsilon v_s}. \tag{23}$$

The first term in the square brackets is the standard lever arm term from a linear voltage drop. The second term results from the charging of the well. If $\tilde{n}_w = 0$, this term is zero. The last term is the impedance of the drift region [9].

As $\omega \to \infty$, Z_{RTD} reduces to $Z_{RTD} = 1/(j\omega C_{ec})$ where $C_{ec} = \epsilon/(l + d + X_c)$ is the emitter-contact to collector-contact capacitance.

In the limit of $v_s \to \infty$, the impedance reduces to that of Feiginov [4] which is Eq. (13) with l replaced by $l + X_c$.

V. Device Simulation

Our test devices are $In_{0.53}Ga_{0.47}As$/InAs/AlAs RTDs. Three structures, consisting of identical quantum-well regions but different barrier thickness, are examined. All devices have $In_{0.53}Ga_{0.47}As$ / InAs / $In_{0.53}Ga_{0.47}As$ wells in which the central InAs layer is 6 monolayers and the cladding $In_{0.53}Ga_{0.47}As$ layers are 5 monolayers. The 10^{19} cm^{-3} doped $In_{0.53}Ga_{0.47}As$ emitter is separated from the emitter barrier by a 5 nm, 10^{15} cm^{-3} doped spacer layer. Three different AlAs barrier thicknesses are modeled: 4, 6 and 8 monolayers. All devices shown have symmetric barriers. We label the devices as 4/4, 6/6, or 8/8 corresponding to their barrier thicknesses. The cross sectional area for all devices is $1\ \mu$m^2. The saturation velocity, v_s, is fixed by the material composition of the drift region and is 5×10^6 cm/s for $In_{0.53}Ga_{0.47}As$ [10], [11].

Table I and II list the parameters from the Matlab and NEMO simulations for the devices. J_0 and G^0 are extracted from the I-V curves of NEMO [12] simulations which use a single band model with a modified mass of 0.08 m_0 for the AlAs barriers which has been found to provide good fits to the experimental current magnitudes. To calculate Z_I in Eq. (13), we require the quantities $\Gamma_0 = \Gamma_e^0 + \Gamma_c^0$, Γ_c', and Γ_e'. We calculate quantum mechanically the quantities Γ_e^0, Γ_c^0, and Γ_c' as describe below. Γ_e' is then chosen to obtain the correct zero frequency conductance, Eq. (14), where it enters through the quantity Γ, Eq. (10).

Γ_c^0 and Γ_e^0 are determined by the transmission coefficients through the corresponding barrier times the attempt rate in the well [13]. $\Gamma_c^0 = \nu |t_{CB}|^2 \frac{k_c}{k_w}$ and $\Gamma_e^0 = \nu |t_{EB}|^2 \frac{k_w}{k_e}$ where k_e, k_w, and k_c are the wavevectors in the emitter, well, and collector at the resonant energy. The attempt rate, ν, is $\nu = \frac{1}{2W}\frac{\hbar}{m_w^*}\frac{\sqrt{2m_w^*(\epsilon - E_{cw})}}{\hbar}$, where m_w is the effective mass in the well.

In order to solve for Γ_c', a bias change V_{cw} is applied (see Fig. 1). $\Gamma_c(V_{cw})$ is solved with the definition for k_i (i = 1, 2, 3) as follows: $k_1(V_{cw}) = \sqrt{2m_1^*\left[\epsilon - \left(E_{c1} - qV_{cw}\frac{W/2}{W/2+t_c}\right)\right]}/\hbar$, $k_2(V_{cw}) = i\sqrt{2m_2^*\left[\left(E_{c2} - qV_{cw}\frac{W/2+t_c/2}{W/2+t_c}\right) - \epsilon\right]}/\hbar$, and $k_3(V_{cw}) = \sqrt{2m_3^*\left[\epsilon - (E_{c3} - qV_{cw})\right]}/\hbar$, where t_c is the collector barrier thickness and W is the width for the QW. Γ_c' is evaluated

numerically from $\Gamma_c' = \frac{\Gamma_c(V_{cw}) - \Gamma_c^0}{V_{cw}}$ where $V_{cw} = 5$ mV. For the calculations above, ϵ, E_{ci} and m_i (i = 1, 2, 3) are taken from the NEMO simulation results.

Now, using the formalism presented above, we investigate the frequency response of the RTDs with different collector drift lengths DC biased in both the PDR and NDR regions. We begin with devices biased in the PDR region. Fig. 3 shows the magnitude (a) and phase (b) of γ for the three devices (4/4, 6/6 and 8/8) DC biased in the PDR region. Comparing to Table I, the frequency at which the $\pi/2$ injection phase occurs increases as the device current density increases. π injection phase is not observed in the PDR region. The injection phase is used to design the drift length such that the device operation is optimized.

Fig. 4 shows the maximized negative resistance that can be obtained in the PDR region at 4 different frequencies (30, 100, 200, 300 GHz). The negative resistance at a given frequency is maximized when the sum of the injection and transit angles is 2π. The injection phase is solely determined by the injection region and is fixed at each frequency, as shown in Fig. (3b). The drift length is designed to create a transit angle such that the sum of the injection and transit angles is 2π. At 30 GHz, huge negative resistances ($|R| > 1600\ \Omega$) are achieved for the 6/6 and 8/8 devices. The 6/6 device has the largest negative resistance at all but the highest and lowest frequencies. At 100 and 200 GHz, its negative resistance is -284 and -47 Ω, respectively. At 300 GHz, the 4/4 device has the maximum negative resistance of -18 Ω. Since a good contact resistance in this system is around 10^{-7} $(\Omega\,\mathrm{cm}^2)$ corresponding to a minimum series resistance of 10 Ω for our 1 $\mu\mathrm{m}^2$ device, the magnitude of the negative resistance should be $> 10\ \Omega$ to generate a net negative resistance across the device terminals. We will use this number as a lower limit when discussing high frequency performance.

Fig. (5), shows the conductance, susceptance, resistance and reactance as a function of frequency for the 6/6 device from Fig. (4) with the 182 nm drift region optimized for a maximum negative resistance at 200 GHz. Note that this is not where the zero derivative point occurs on the R vs. f curve, Fig. (5c). However, when we modify the drift region such that the zero derivative point occurs at 200 GHz, the magnitude of the negative resistance at 200 GHz is less than that obtained from the choice of X_c here such that the sum of the injection and transit angles are exactly 2π at 200 GHz.

The magnitude and phase for γ in the NDR region is shown in Fig. 6. The phase starts at zero, goes negative, and then increases, finally saturating around $\pi/2$. Figs. (7a,b,c) show details

of the frequency response of the resistance and conductance of the 6/6 device DC biased in the NDR region with five different drift lengths: 0, 20, 40, 60 and 206 nm. The frequency roll off of the negative resistance is rapid. For example, the device with a 40 nm drift region starts with a negative resistance of -1.3 kΩ which falls to one half of that value at a frequency of 36 GHz. Increasing the collector drift region length initially increases the negative resistance. However, as shown in Figs. (7a,b), as the frequency increases, there is a cross-over such that at the highest frequencies, the device with the shortest collector drift region has the largest negative resistance. The general trend is that the resistance increases, crosses zero, becomes positive, then decreases due to transit time effects and has a negative minimum as shown for the 206 nm device in Fig. (7b). In all cases, we find that the magnitude of the negative resistance at this minimum is never larger than that obtained from a much shorter device whose resistance has not yet crossed zero such as the 20 nm device in Fig. (7b). However, the 206 nm device has a much larger voltage swing, ΔV, than the 20 nm device, approximately 10 times as large, so the millimeter wave power at the resistance minimum could be 10 times larger for the 206 nm device compared to the 20 nm device.

The rapid roll-off of the negative resistance may seem initially surprising considering that the intrinsic inverse lifetime $\Gamma^0 = 1.9$ THz and the inverse dwell time $\Gamma = 1.8$ THz. However, the dwell time governs the roll off of the conductance as shown in Eq. (13). The conductance of the 6/6 device with a 0-length drift region falls to 1/2 of its DC value at 475 GHz. The fast roll-off of the resistance is the result of the almost linear increase in susceptance with frequency from the $j\omega C_{e0}$ term in Eq. (13). For conductance G and susceptance ωB, the resistance is $R = G/\left[G^2 + (\omega B)^2\right]$. For all of our devices, the susceptance is one to two orders of magnitude larger than the conductance by the time the frequency reaches 100 GHz resulting in the rapid fall off of the negative resistance.

Figs. 8 and 9 examine devices 4/4 and 8/8 in the NDR region, respectively. Device 4/4, DC biased in the NDR region, results in the largest negative resistance at the highest frequency of all of the devices and biasing that we have studied. At 400 GHz, the resistance of the 20 nm device drops to slightly under -17 Ω. The 10 nm device falls to approximately -10 Ω at 500 GHz. At 300 GHz, the negative resistance of the 20 nm device is -31 Ω. This should be compared with the -18 Ω of the 4/4 device DC biased in the PDR region. The PDR biased device has a larger drift region (*140 nm*, see Table III) resulting in a larger voltage swing ΔV. Thus the PDR biased

device can potentially generate larger millimeter wave power than the NDR biased device with the shorter drift region.

The same trends occur in the 8/8 device at much lower frequencies and longer drift lengths as shown in Fig. 9. Finally, we note that we investigated the effect of using asymmetric barriers on the magnitude and frequency response of the negative resistance for DC biasing in both the PDR and NDR regions. We found no significant advantage or disadvantage resulting from asymmetric barrier devices. For the PDR biased devices, barrier asymmetry had no significant effect on the injection phase angle.

In summary, we have presented a self-consistent small-signal AC model for an RTD with a collector drift region and analyzed the effect of the drift region length on the frequency dependence of the resistance and conductance. Devices DC biased in the PDR region demonstrate dynamical negative resistance of -284 Ω at 100 GHz, -47 Ω at 200 GHz, and -18 Ω at 300 GHz. The largest negative resistance at the highest frequencies is obtained from the high current density device (4/4) biased in the NDR region with relatively short collector drift regions of 10 and 20 nm. The 20 nm device falls to -17 Ω at 400 GHz and the 10 nm device falls to -10 Ω at 500 GHz. Barrier asymmetry has little effect on the magnitude and frequency response of the negative dynamical resistance.

REFERENCES

[1] V. P. Kesan, D. P. Neikirk, B. G. Streetman, and P. A. Blakey, "A new transit-time device using quantum-well injection," *IEEE Elect. Dev. Lett.*, vol. EDL-8, no. 4, pp. 129–131, 1987.

[2] V. P. Kesan, D. P. Neikirk, P. A. Blakey, B. G. Streetman, and T. D. Linton, "The influence of transit-time effects on the optimum design and maximum oscillation frequency of quantum well oscillators," *IEEE Trans. Elect. Dev.*, vol. 35, no. 4, pp. 405–413, 1988.

[3] S. Yngvesson, *Microwave Semiconductor Devices*. Boston: Kluwer Academic, 1991.

[4] M. N. Feiginov, "Displacement currents and the real part of the high-frequency conductance of the resonant-tunneling diode," *Appl. Phys. Lett.*, vol. 78, no. 21, pp. 3301–3, 2001.

[5] E. R. Brown, W. D. Goodhue, and T. C. L. G. Sollner, "Fundamental oscillations up to 200 ghz in resonant tunneling diodes and new estimates of their maximum oscillation frequency from stationary-state theory,," *J. Appl. Phys.*, vol. 64, no. 3, pp. 1519–1528, 1988.

[6] A. Botula and K. L. Wang, "Improved small-signal analysis of the quantum-well injection transit time diode," *IEEE Trans. Elect. Dev.*, vol. 37, no. 1, pp. 58–66, 1990.

[7] E. R. Brown, C. D. Parker, and T. C. L. G. Sollner, "Effect of quasibound-state lifetime on the oscillation power of resonant tunneling diodes," *Appl. Phys. Lett.*, vol. 54, no. 10, pp. 934–6, 1989.

[8] R. Lake and J. Yang, "A physics based model for the rtd quantum capacitance," *IEEE Trans. Elect. Dev.*, vol. 50, no. 3, pp. 785–9, 2003.

[9] S. M. Sze, *Physics of Semiconductors*, 2nd ed. New York: John Wiley and Sons, 1981.

[10] S. Adachi, "Gaas, alas, $al_x ga_{1-x} as$: material parameters for use in research and device applications," *J. Appl. Phys.*, vol. 58, no. 3, pp. R1–R29, 1985.

[11] T. H. Windhorn, L. W. Cook, and G. E. Stillman, "The electron velocity field characteristic for n-$in_{0.53} ga_{0.47} as$ at 300k," *IEEE Elect. Dev. Lett.*, vol. 3, no. 1, 1982.

[12] D. K. Blanks, G. Klimeck, R. Lake, D. Jovanovic, R. C. Bowen, C. Fernando, W. R. Frensley, and M. Leng, "Nemo: general release of a new comprehensive quantum device simulator," in *Compound Semiconductors 1997. Proceedings of the IEEE Twenty-Fourth International Symposium on Compound Semiconductors*. New York: IEEE, 1998, pp. 639–642.

[13] R. Lake, G. Klimeck, and S. Datta, "Rate equations from the keldysh formalism applied to the phonon peak in resonant tunneling diodes," *Phys. Rev. B*, vol. 47, no. 11, pp. 6427–38, 1993.

Figure Captions

1. The band diagram and model charge distribution of an RTD.

2. RLC circuit model for the injection region.

3. The phase and magnitude for γ in the PDR region.

4. Maximized negative resistances at 30, 100, 200 and 300 GHz in the PDR region.

5. (a) Conductance, (b) Susceptance, (c) Resistance, and (d) Reactance vs. frequency of 6/6 device with 182 nm drift length.

6. The phase and magnitude for γ in the NDR region.

7. Resistance and conductance for device 6/6 in the NDR region.

8. Resistance for device 4/4 in the NDR region.

9. Resistance for device 8/8 in the NDR region.

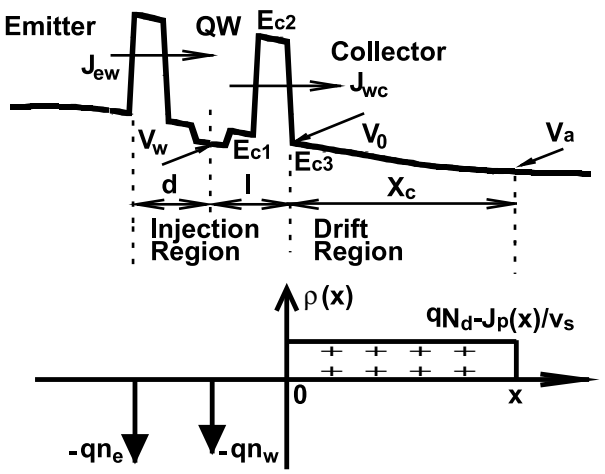

Fig. 1. Y. Zheng and R. Lake, IEEE Trans. Elect. Dev.

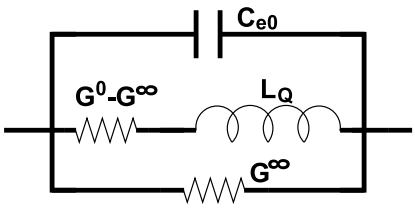

Fig. 2. Y. Zheng and R. Lake, IEEE Trans. Elect. Dev.

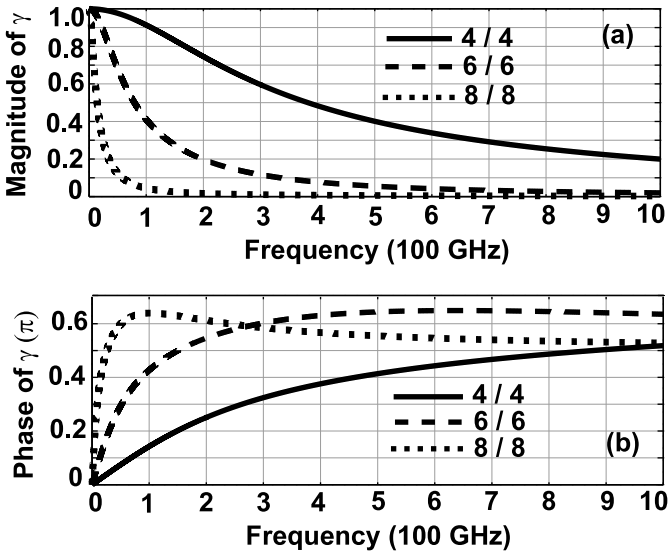

Fig. 3. Y. Zheng and R. Lake, IEEE Trans. Elect. Dev.

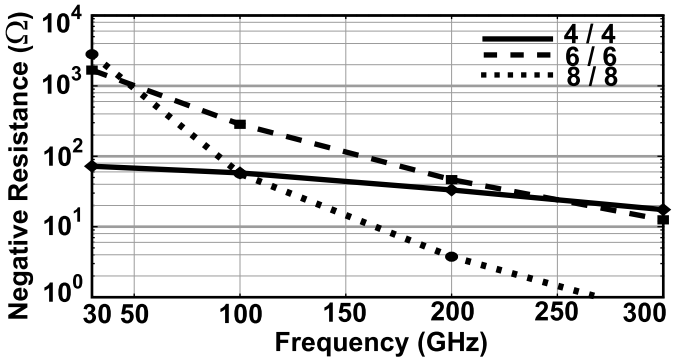

Fig. 4. Y. Zheng and R. Lake, IEEE Trans. Elect. Dev.

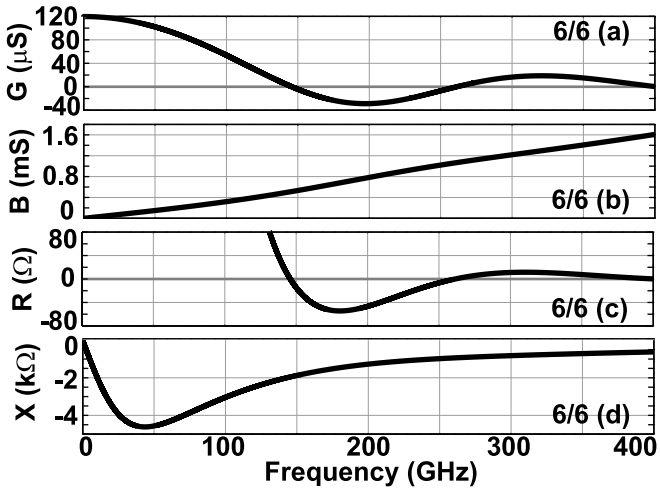

Fig. 5. Y. Zheng and R. Lake, IEEE Trans. Elect. Dev.

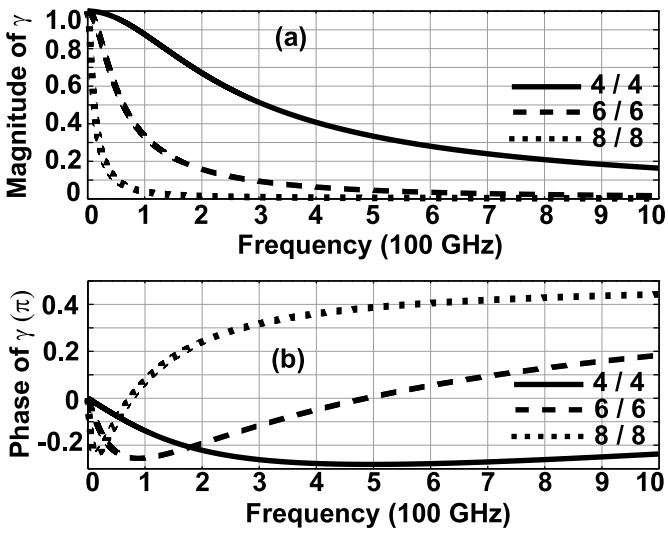

Fig. 6. Y. Zheng and R. Lake, IEEE Trans. Elect. Dev.

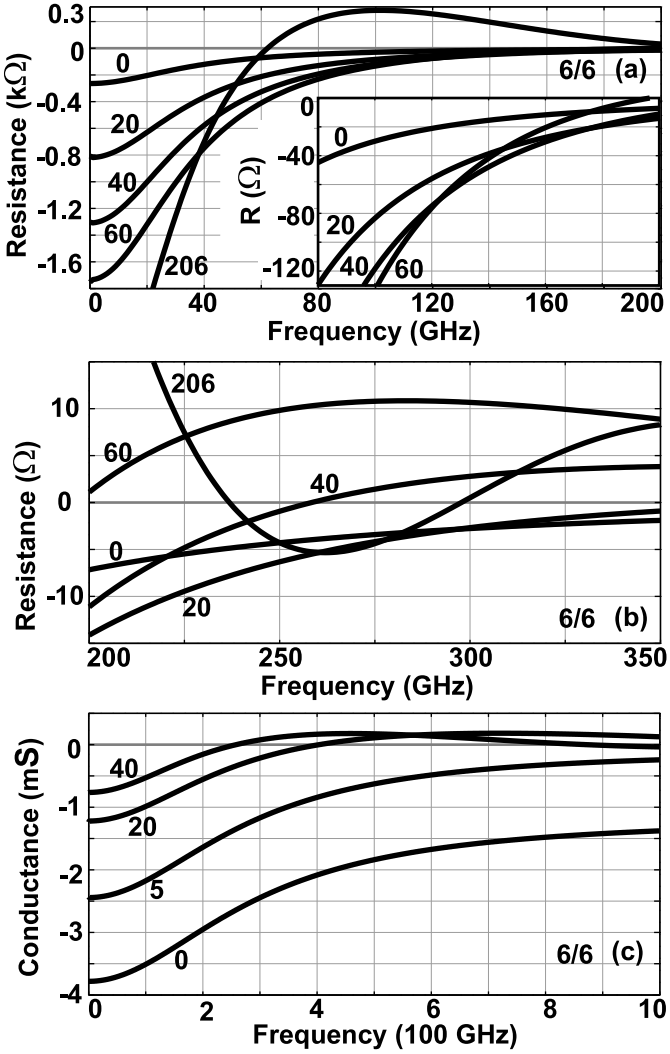

Fig. 7. Y. Zheng and R. Lake, IEEE Trans. Elect. Dev.

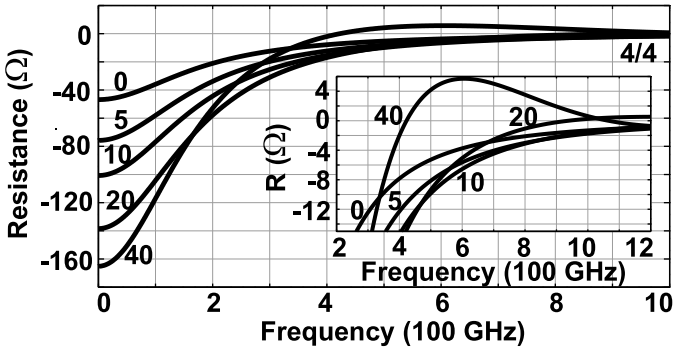

Fig. 8. Y. Zheng and R. Lake, IEEE Trans. Elect. Dev.

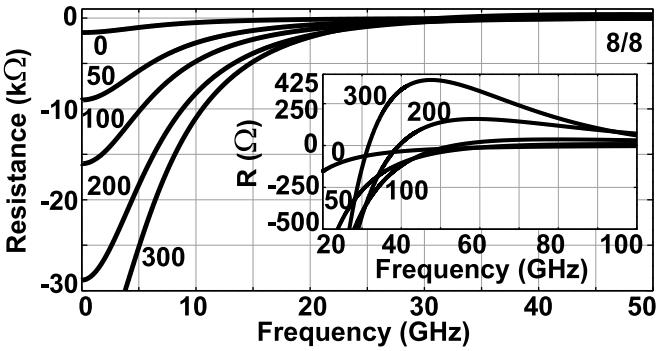

Fig. 9. Y. Zheng and R. Lake, IEEE Trans. Elect. Dev.

TABLE I

PARAMETERS IN THE PDR REGION

Device	$J_0\ (mA)$	$G^0\ (mS)$	$G^\infty\ (mS)$	$\Gamma\ (THz)$	$\Gamma_0\ (THz)$	$\Gamma_c^0\ (THz)$	$\Gamma_e^0\ (THz)$	$\Gamma_c'\ (\frac{THz}{V})$	$\Gamma_e'\ (\frac{THz}{V})$
4/4	4.389	24.29	19.50	12.21	11.10	8.853	2.246	39.72	-10.42
6/6	0.611	4.352	3.533	1.963	1.728	1.314	0.414	6.079	-0.766
8/8	0.095	0.681	0.561	0.313	0.271	0.205	0.066	0.995	0.035

TABLE II

PARAMETERS IN THE NDR REGION

Device	$J_0\ (mA)$	$G^0\ (mS)$	$G^\infty\ (mS)$	$\Gamma\ (THz)$	$\Gamma_0\ (THz)$	$\Gamma_c^0\ (THz)$	$\Gamma_e^0\ (THz)$	$\Gamma_c'\ (\frac{THz}{V})$	$\Gamma_e'\ (\frac{THz}{V})$
4/4	4.247	-21.36	-6.483	11.92	12.29	12.04	0.255	43.1	-3.013
6/6	0.658	-3.782	-1.170	1.842	1.920	1.873	0.047	7.117	-0.620
8/8	0.100	-0.626	-0.185	0.288	0.302	0.297	0.005	1.235	-0.065

TABLE III

$X_c(nm)$ FOR EACH DEVICE AND FREQUENCY IN FIG. 4

Device	f (GHz)			
	30	100	200	300
4/4	1629	464	219	140
6/6	1500	393	182	116
8/8	1229	340	173	118